ARTICLE NO. 77-132R

J80-071

Unsteady Potential Aerodynamics of Rotors with Applications to Horizontal-Axis Windmills

10029
20005
20009

Robert D. Preuss,* Emil O. Suciu,† and Luigi Morino‡
Boston University, Boston, Mass.

The problem of a horizontal-axis windmill in incompressible, potential flow is considered. The problem is formulated in a frame of reference rigidly connected with the rotor. Two different integral equations (for finite-thickness and zero-thickness blades) are presented. The finite-thickness integral equation relates the values of the potential on the surface of the windmill to the values of the normal derivative, which are known from the boundary conditions. The wake is treated as a doublet layer of prescribed helicoidal geometry. In order to solve the integral equation, the windmill surface is divided into small quadrilateral surface elements. Each element is approximated by a portion of a hyperboloidal paraboloid passing through the corners of the actual surface element. The values of the potential and its normal derivative within each element are assumed to be constant and equal to the values at the centroid of the element. This yields a set of linear algebraic equations in the unknown values of the potential. The zero-thickness integral equation is treated in a similar way. Numerical results for potential and power coefficient for finite-thickness and zero-thickness horizontal-axis windmills in steady and unsteady incompressible, potential flows are presented. Comparison with experiment is presented for helicopter rotors in hover.

Nomenclature

a^α, a_α = contravariant and covariant base vectors
$a^{\alpha\beta}, a_{\alpha\beta}$ = contravariant and covariant components of the metric tensor
c_p = pressure coefficient
c_P = power coefficient
d = length of wake spiral
n = unit normal
p = pressure
P = power
P = point in rotating Cartesian space
P_0 = control point
q = dynamic pressure
R = rotor radius
S = rotor disk area
t = time
U_∞ = time mean uniform coaxial component of V_∞
U_0 = zero-power value of U_∞
V_∞ = unperturbed fluid velocity as seen from rotating frame of reference
V_W = unperturbed fluid velocity in rotating frame of reference
V_R = rotor velocity in rotating frame of reference
V_F = fluid velocity in rotating frame of reference
δ_{hk} = Kronecker delta
θ = blade twist angle
ξ^α = curvilinear coordinates
π = perturbation vector potential
ρ = fluid density
Σ_w = wake surface
Σ_R = rotor surface
Σ = $\Sigma_R + \Sigma_w$
σ = surface element
τ = delay time
ϕ = perturbation scalar potential
$\tilde{\phi}$ = Nth coefficient of Fourier series in time for ϕ
Ω = angular velocity of rotating frame of reference
∇ = gradient operator

Presented as Paper 77-132 at the AIAA 15th Aerospace Sciences Meeting, Los Angeles, Calif., Jan. 24-26, 1977; submitted March 9, 1977; revision received Aug. 8, 1979.

Index categories: Wind Power; Computational Methods; Nonsteady Aerodynamics.

*Research Assistant. Currently, Project Leader, MITRE Corp., Bedford, Mass. Member AIAA.

†Research Assistant. Currently, Engineer Load and Dynamics Group, Gates Learjets Corp., Wichita, Kansas. Member AIAA.

‡Research Professor of Aerospace and Mechanical Engineering. Director, Center for Computational and Applied Dynamics. Member AIAA.

I. Introduction

THE recent energy crisis has brought about a renewed interest in obtaining energy from sources other than fossil fuels. Among the other available sources, one which has been used for thousands of years is wind energy. A strong effort is now underway to develop the appropriate technology required to design large-scale wind turbines. In particular, the structural dynamics of the rotor blades is a very complex problem to analyze. Especially difficult is the evaluation of the aerodynamic pressure, since the flowfield is very complex due to various problems such as wind shear, tower shadow, and wake rollup in a rotating system. The purpose of this paper is to present results obtained in the development of two general methods for the aerodynamic analysis of rotors with application to wind turbines. The details of the present effort are presented in Ref. 1 and include the unsteady nonpotential analysis of the effects of the presence of the flowfield vorticity (such as the one due to wind shear, tower shadow, or boundary layer) while the long-range goals are presented in Ref. 2. The present paper is limited to horizontal-axis windmills in potential flows.

In order to put the work presented here in the proper perspective, it is appropriate to make a short review of the state-of-the-art in theoretical windmill aerodynamics. This subject was originated by the pioneering works of Rankine,[3] Froude,[4,5] Betz,[6] and Drzewiecki[7] on blade-element and momentum theories. Glauert[8] gives an excellent review of these and other early works on windmill aerodynamics. Since then, there has been very little activity in this field, until the recent energy crisis has renewed the interest in the use of

windmills for power production. Recently, Wilson and Lissaman[9] and Wilson et al.[10] have introduced improved methods of analysis for propeller-type windmills which are based on classical concepts. Classical theoretical analysis for horizontal-axis windmills is compared to experimental data in Ref. 11. Finally a lifting-surface analysis of rotors, with emphasis on helicopters and propellers, is given in Refs. 12 and 13.

In this paper two methods are presented. The simpler one is a lifting-surface analysis in which the rotor and its wake are treated as doublet layers. This is an extension to rotors of the analysis presented in Ref. 14. In the second method, for complex configurations, the actual finite-thickness geometry of the rotor is used. The surface of the hub can be included without any modification of the program. The complex configuration method is an extension of the Green's function method developed in Refs. 15 and 16. The theoretical and numerical formulations are briefly outlined in Secs. III, IV, and V. Numerical results are presented in Sec. VI.

II. Basic Equations

Consider a frame of reference rotating with constant angular velocity Ω around an axis parallel to the x axis. The solution will be time dependent if the equations are expressed in a frame of reference connected with the ground, but time independent if a coordinate system rigidly connected with the rotor is used and the flow is uniform and coaxial. The equations for incompressible potential flows in the frame of reference rigidly connected with the rotor are obtained in Ref. 1 and are briefly presented here. Let the fluid velocity be given by

$$\boldsymbol{V}_F = \boldsymbol{V}_W + \nabla\phi + \nabla \times \boldsymbol{\pi} \tag{1}$$

where the velocity of the unperturbed wind in the rotating frame of reference, $\boldsymbol{V}_W$, is given by

$$\boldsymbol{V}_W = \boldsymbol{V}_\infty - \Omega \boldsymbol{i} \times \boldsymbol{P} \tag{2}$$

where $\boldsymbol{P}$ is any point in the rotating frame of reference and $\boldsymbol{V}_\infty$ is the unperturbed flow velocity as seen in the rotating frame of reference. Note that the problem is generally nonpotential (e.g., shear winds). A significant mathematical simplification is obtained if the flow is inviscid and the vorticity present in the unperturbed flow is not significantly disturbed by the presence of the windmill. In this case the perturbation vector potential $\boldsymbol{\pi}$ is negligible and the fluid velocity is

$$\boldsymbol{V}_F = \boldsymbol{V}_W + \nabla\phi \tag{3}$$

A further simplification is obtained when $\boldsymbol{V}_\infty = U_\infty \boldsymbol{i}$ (where U_∞ is the time mean uniform coaxial component of the unperturbed flow velocity) which specializes the problem to the steady-state case.

The differential equation for the velocity perturbation potential ϕ is

$$\nabla^2\phi = 0 \tag{4}$$

with $\phi = 0$ for $\boldsymbol{P}$ at infinity.

The boundary condition on the surface of the rotor is that the fluid does not penetrate the surface, or

$$\boldsymbol{V}_F \cdot \boldsymbol{n} = \boldsymbol{V}_R \cdot \boldsymbol{n} \tag{5}$$

where $\boldsymbol{n}$ is the normal to the rotor surface and $\boldsymbol{V}_R$ is the velocity of a point on the surface of the rotor.

Combining Eqs. (3) and (5), the boundary condition becomes, in terms of the perturbation potential,

$$\frac{\partial\phi}{\partial n} = -\boldsymbol{V}_W \cdot \boldsymbol{n} + \boldsymbol{V}_R \cdot \boldsymbol{n} \tag{6}$$

The Bernoulli's theorem in the rotating frame of reference gives the expression for the pressure coefficient as

$$c_p = \frac{p - p_\infty}{\frac{1}{2}\rho U_\infty^2} = \frac{2}{U_\infty^2}\left(\frac{\partial\phi}{\partial t} + \boldsymbol{V}_w \cdot \nabla\phi + \frac{1}{2}|\nabla\phi|^2\right) \tag{7}$$

The boundary condition on the wake surface is that there is no pressure discontinuity across the wake, or, using Eq. (7)

$$\Delta\phi(\boldsymbol{P}_{\text{wake}}, t) = \text{const} \tag{8}$$

following a wake particle, i.e.,

$$\Delta\phi(\boldsymbol{P}_{\text{wake}}, t) = \Delta\phi(\boldsymbol{P}_{TE}, t - \tau) \tag{9}$$

where $\boldsymbol{P}_{TE}$ is the point on the rotor trailing edge from which the wake particle at $\boldsymbol{P}_{\text{wake}}$ emanated and τ is the time taken for the particle to travel from $\boldsymbol{P}_{TE}$ to $\boldsymbol{P}_{\text{wake}}$.

III. Formulation for Finite-Thickness Blades

Using the classical Green's function approach as presented in Ref. 15, Eq. (4) is transformed into an integral equation

$$2\pi\phi(\boldsymbol{P}_0) = -\oiint_{\Sigma_R} \frac{\partial\phi}{\partial n}\frac{1}{r}\,d\Sigma_R + \oiint_{\Sigma_R} \phi\frac{\partial}{\partial n}\left(\frac{1}{r}\right)d\Sigma_R + \iint_{\Sigma_w} \Delta\phi\frac{\partial}{\partial n_1}\left(\frac{1}{r}\right)d\Sigma_w \tag{10}$$

Here Σ_w is the (open) surface of the wake and Σ_R is the (closed) surface surrounding the rotor, whereas, in the integral over Σ_w, n_1 is the normal to the side 1 of Σ_w and $\Delta\phi = \phi_1 - \phi_2$.

For simplicity, the geometry of the wake is considered to be prescribed and is approximated here by a fixed helicoidal surface [see Eq. (40)]. $\partial\phi/\partial n$ is known from the boundary condition, Eq. (6). Thus, the problem is completely described by Eqs. (6), (9), and (10) while the pressure coefficient may be evaluated using Eq. (7). Note that on the surface Σ_R, the perturbation velocity is given by

$$\nabla\phi = \frac{\partial\phi}{\partial\xi^1}\boldsymbol{a}^1 + \frac{\partial\phi}{\partial\xi^2}\boldsymbol{a}^2 + \frac{\partial\phi}{\partial n}\boldsymbol{n} \tag{11}$$

where ξ^α are curvilinear coordinates on Σ_R, $\boldsymbol{a}^\alpha$ and $\boldsymbol{n}$ the contravariant base vectors and the unit normal on Σ_R [see Eq. (30)]. It should be noted that $\partial\phi/\partial n$ is known from the boundary conditions whereas $\partial\phi/\partial\xi^\alpha$ may be evaluated from ϕ once Eq. (10) has been solved.

Consider now the problem of solving Eq. (10) numerically. Two types of unsteady analysis will be described here: the oscillatory unsteady analysis and the transient unsteady analysis. For both types of analysis the surface Σ_R is divided into small elements, σ_k. The values of ϕ and $\partial\phi/\partial n$ are assumed to be constant within and equal to the value ϕ_k and $(\partial\phi/\partial n)_k$ at the centroid of each element. The wake is divided into helicoidal strips emanating from elements in contact with the trailing edge and each strip is divided into elements, σ_m^*. The collocation method is then used, that is, Eq. (10) is satisfied at the centroid, $\boldsymbol{P}_h$, of the element σ_h. This yields

$$[\delta_{hk} - c_{hk}]\{\phi_k\} = [b_{hk}]\left\{\left(\frac{\partial\phi}{\partial n}\right)_k\right\} + [f_{hm}]\{(\Delta\phi)_m\} \tag{12}$$

where δ_{hk} is the Kronecker delta, and

$$c_{hk} = \left[\frac{1}{2\pi}\iint_{\sigma_k}\frac{\partial}{\partial n}\left(\frac{1}{r}\right)d\sigma_k\right]_{P_0 = P_h} \tag{13}$$

$$b_{hk}=\left[\frac{-1}{2\pi}\iint_{\sigma_k}\frac{1}{r}\mathrm{d}\sigma_k\right]_{P_0=P_h} \tag{14}$$

$$f_{hm}=\left[\frac{1}{2\pi}\iint_{\sigma_m^*}\frac{\partial}{\partial n_1}\left(\frac{1}{r}\right)\mathrm{d}\sigma_m\right]_{P_0=P_h} \tag{15}$$

Each surface element of the rotor and its wake is approximated by a portion of a hyperboloidal paraboloid interpolating the four corner points; exact expressions for the b_{hk}, c_{hk}, and f_{hm} coefficients are given in Refs. 17 and 18.

For the oscillatory unsteady analysis, ϕ and $\partial\phi/\partial n$ are expressed as complex Fourier series in time. The linearity of Eq. (10) together with the linear independence of the complex exponentials in the Fourier series implies that Eq. (10) is true for each coefficient of the Fourier series. The boundary condition on the wake for the Nth coefficient of the Fourier series is [see Eq. (9)]

$$\Delta\tilde{\phi}(\boldsymbol{P}_{\text{wake}})=\Delta\tilde{\phi}(\boldsymbol{P}_{TE})e^{-i\omega N\tau} \tag{16}$$

where $\boldsymbol{P}_{TE}$ is the point on the trailing edge of the rotor surface from which $\boldsymbol{P}_{\text{wake}}$ emanates and τ is the propagation time from $\boldsymbol{P}_{TE}$ to $\boldsymbol{P}_{\text{wake}}$. For each strip, $\Delta\tilde{\phi}(\boldsymbol{P}_{TE})$ is approximated by the difference in values at the centroids of elements on either side of the blade in contact with the trailing edge, while τ is approximated by $x_{\text{wake}}-x_{TE}$ divided by U_∞. The preceding approximations yield [from Eq. (12)] a system of algebraic equations with frequency dependent coefficients, which is then solved for $\tilde{\phi}_k$, the coefficient of the Nth term in the Fourier series for the potential.

For the transient unsteady analysis, the wake is still divided into strips emanating from elements of Σ_R in contact with the trailing edge. Each wake strip is then divided into elements in such a way that the propagation delay time from the trailing edge to each division of the strip is an integer multiple of a small prescribed time step, Δt. In this case the potential discontinuity at the wake strip divisions at the present time is known from the boundary conditions [Eq. (9)]. Equation (12) may now be interpreted as yielding the potential distribution on Σ_R at the present time in terms of the potential discontinuity on Σ_w at the present time [which, from Eq. (9), is given by the trailing-edge potential discontinuity at the previous times] and the boundary condition, Eq. (6), at the present time. The potential discontinuity within each wake element is approximated by the average of its values at the upstream and downstream edges of the element. Once Eq. (12) has been solved the potential distribution on Σ_R is known at the present time and the foregoing procedure may be repeated to obtain the solution at future times.

It should be noted that the oscillatory analysis requires that the wake be of fixed geometry, since the algebraic equation for the spatially discretized time independent coefficient in the Fourier series for ϕ must be time independent and the matrix operator involves integrals dependent upon the wake geometry. However, the transient analysis has no such requirement and may be used to include the effect of the variation of the wake geometry.

IV. Formulation for Zero-Thickness Blades

If the distance between the upper and lower sides of the blade surface goes to zero (zero-thickness blades), Eq. (10) reduces to

$$\phi(\boldsymbol{P}_0)=\iint_\Sigma\frac{\Delta\phi}{4\pi}\frac{\partial}{\partial n_1}\left(\frac{1}{r}\right)\mathrm{d}\Sigma \tag{17}$$

where Σ extends over the lifting surface and its wake and

$$\Delta\phi=\phi_1-\phi_2 \tag{18}$$

(where the subscripts 1 and 2 stand for the two sides of the surface) and $\boldsymbol{n}_1$ is the normal to side 1 of the surface. Equation (17) shows that the potential can be represented by a doublet distribution on the rotor blades and on the wake.

For simplicity, only the solution for the steady state is discussed here. Extension to the unsteady state may be made along the lines of the procedure outlined for the finite-thickness blade formulation.

For steady state, the value of $\Delta\phi$ is constant along the streamlines of the wake and equal to its value at the trailing edge of the blade [see Eq. (9)].

The boundary condition, Eq. (6), must be satisfied. Using Eq. (17), the following integral equation results:

$$\frac{\partial\phi}{\partial n_0}=\iint_\Sigma\frac{\Delta\phi}{4\pi}\frac{\partial^2}{\partial n_0\partial n_1}\left(\frac{1}{r}\right)\mathrm{d}\Sigma \tag{19}$$

where $\partial\phi/\partial n_0$ (the subscript zero denotes the control point) is known and given by Eq. (6). The surface of the wake is assumed to be helicoidal [see Eq. (40)].

After Eq. (19) has been solved for $\Delta\phi$, the velocity at any point $\boldsymbol{P}$ in the field, may be obtained from Eq. (3) with

$$\nabla\phi=\nabla\iint_\Sigma\frac{\Delta\phi}{4\pi}\frac{\partial}{\partial n_1}\left(\frac{1}{r}\right)\mathrm{d}\Sigma \tag{20}$$

From $\nabla\phi$, the pressure is obtained by using Bernoulli's theorem, Eq. (7).

In order to obtain an approximate solution of Eq. (19), the lifting surface and its wake (of known geometries) are divided into small surface elements. Assume that the value of $\Delta\phi$ is constant within each element and equal to the value $\Delta\phi_k$ at the centroid of the element σ_k. Then Eq. (19) reduces to

$$\frac{\partial\phi}{\partial n_0}=\Sigma_k\frac{\Delta\phi_k}{4\pi}\iint_{\sigma_k'}\frac{\partial^2}{\partial n_0\partial n_1}\left(\frac{1}{r}\right)\mathrm{d}\sigma_k' \tag{21}$$

where, for the elements in contact with the wake, σ_k' is equal to σ_k plus the wake strip emanating from σ_k (with the same normal), whereas $\sigma_k'\equiv\sigma_k$ otherwise. Note that $\Delta\phi$ is constant along streamlines of the wake and equal to its value at the trailing edge or approximately equal to $\Delta\phi$ at the centroids of the blade elements in contact with the trailing edge (see also discussion of Fig. 3). If we impose that the boundary condition, Eq. (6), is satisfied at the centroids $\boldsymbol{P}_h$ of the blade surface elements σ_h, the following system of linear algebraic equations is obtained:

$$[A_{hk}]\{\Delta\phi_k\}=\{B_h\} \tag{22}$$

where

$$A_{hk}=\left[\iint_{\sigma_k'}\frac{\partial^2}{\partial n_0\partial n_1}\left(\frac{1}{r}\right)\mathrm{d}\sigma_k'\right]_{P_0=P_h} \tag{23}$$

and

$$B_h=4\pi\left(\frac{\partial\phi}{\partial n_0}\right)_{P_0=P_h} \tag{24}$$

In addition, note that Eq. (11) cannot be used to evaluate $\nabla\phi$ since only $\Delta\phi$ (not ϕ) is evaluated in the lifting surface formulation. Therefore $\nabla\phi$ is evaluated by approximating Eq. (20) as

$$\nabla\phi_h=\Sigma_k\frac{\Delta\phi_k}{4\pi}V_{hk} \tag{25}$$

where

$$V_{hk}=\left[\nabla\iint_{\sigma_k'}\frac{\partial}{\partial n_1}\left(\frac{1}{r}\right)\mathrm{d}\sigma_k'\right]_{P_0=P_h} \tag{26}$$

Note that, by definition,

$$A_{hk} = \boldsymbol{n}_h \cdot \boldsymbol{V}_{hk} \tag{27}$$

Therefore, the evaluation of V_{hk} does not require any additional computation.

V. Pressure and Power Coefficient

From Bernoulli's theorem, Eq. (7), the pressure can be obtained if $\nabla\phi$ is known. However, the integral equations giving the distribution of the potential are approximated by algebraic equations which yield the values of the potential only at discrete points. The procedure to evaluate $\nabla\phi$ using these values of the potential is briefly described here. Consider finite-thickness blades first; in this case $\nabla\phi$ is obtained from Eq. (11). First, consider the evaluation of the quantities a^α: the actual surface element is approximated by a hyperboloidal element defined by

$$\boldsymbol{P} = \boldsymbol{P}_c + \boldsymbol{P}_1\xi^1 + \boldsymbol{P}_2\xi^2 + \boldsymbol{P}_3\xi^1\xi^2 \tag{28a}$$

$$-1 \le \xi^1, \quad \xi^2 \le +1 \tag{28b}$$

The four corner points ($\xi^1 = \pm 1$ and $\xi^2 = \pm 1$) are known from the geometry of the problem and from these $\boldsymbol{P}_c, \boldsymbol{P}_1, \boldsymbol{P}_2$, and $\boldsymbol{P}_3$ are found (see Ref. 16). Next, consider the base vectors in the coordinates ξ^1, ξ^2

$$\boldsymbol{a}_1 = \frac{\partial \boldsymbol{P}}{\partial \xi^1}, \quad \boldsymbol{a}_2 = \frac{\partial \boldsymbol{P}}{\partial \xi^2} \tag{29}$$

The contravariant base vectors $\boldsymbol{a}^\alpha$ are given by§

$$\boldsymbol{a}^\alpha = a^{\alpha\beta}\boldsymbol{a}_\beta \tag{30}$$

where the contravariant components of the metric tensor, $a^{\alpha,\beta}$ are defined by

$$a^{\alpha\beta}a_{\beta\gamma} = \delta^\alpha_\gamma \tag{31}$$

with the covariant components of the metric tensor given by

$$a_{\alpha\beta} = \boldsymbol{a}_\alpha \cdot \boldsymbol{a}_\beta \tag{32}$$

Next consider the derivatives $\partial\phi/\partial\xi^\alpha$. In order to obtain a continuous distribution for ϕ, the potential at the corners of the surface elements is evaluated as the average of the values of the potential at the centroids of adjacent elements. Then the velocity potential ϕ at any point within the surface element is interpolated as

$$\phi = \phi_c + \phi_1\xi^1 + \phi_2\xi^2 + \phi_3\xi^1\xi^2 \tag{33}$$

with the same ξ^1 and ξ^2 used in Eq. (28).

The derivatives of the potential are evaluated from Eq. (33) and used in Eq. (11). The pressure coefficient is then evaluated from Eq. (7).

A slightly different procedure is used for calculating the pressure on a zero-thickness blade (see also Ref. 17). Equation (19) gives the distribution of $\Delta\phi$ on the blade surface. From this the pressure discontinuity on the lifting surface is evaluated. This is obtained from the Bernoulli's theorem, Eq. (7), as (see Ref. 17)

$$c_l = (2/U_\infty^2)\,(\boldsymbol{V}_w \cdot \Delta\boldsymbol{v} + \boldsymbol{v}_a \cdot \Delta\boldsymbol{v}) \tag{34}$$

where $\boldsymbol{v}_a = \tfrac{1}{2}\nabla(\phi_1 + \phi_2)$ and $\Delta\boldsymbol{v} = \nabla(\phi_1 - \phi_2)$.

§Einstein's convention on repeated indices is used here. The indices range from 1 to 2.

Equation (25) is used to evaluate the average perturbation velocity $\boldsymbol{v}_a$ at the centroids of the elements. The perturbation velocity discontinuity $\Delta\boldsymbol{v}$ on the lifting surface is obtained by using a procedure similar to the one described for finite-thickness blades, Eqs. (28-33).

Once the pressure has been obtained at the centroids of the blade surface elements, the expression for the power generated by the windmill is

$$P = -\Omega \iint_{\Sigma_R} p\boldsymbol{n}\cdot\boldsymbol{i}\times\boldsymbol{r}\,\mathrm{d}\Sigma_R \tag{35}$$

Dividing the surface into the elements σ_k and noting that

$$\int_{-1}^{+1}\int_{-1}^{+1} \mathrm{d}\xi^1\mathrm{d}\xi^2 = 4 \tag{36}$$

the power coefficient is evaluated as

$$c_P = \frac{P}{qSU_\infty} = -\Sigma_k 4p_k\,(|\boldsymbol{a}_1\times\boldsymbol{a}_2|\boldsymbol{n}\cdot\boldsymbol{i}\times\boldsymbol{P})_{P=P_k}\frac{\Omega}{qSU_\infty}$$

$$= \frac{-4}{q\pi R^2}\frac{\Omega R}{U_\infty}\Sigma_k p_k\left[\boldsymbol{a}_1\times\boldsymbol{a}_2\cdot\frac{\boldsymbol{i}\times\boldsymbol{P}}{R}\right]_{P=P_k} \tag{37}$$

where $\Omega R/U_\infty$ is the tip speed over wind speed ratio.

VI. Numerical Results

The complex-configuration formulation presented in Sec. III has been implemented into a computer program, WICCA (WECS Incompressible Complex Configuration Aerodynamics; WECS being an acronym for Wind Energy Conversion Systems) and the lifting-surface formulation of Sec. IV has been implemented into the computer code WILSA (WECS Incompressible Lifting-Surface Aerodynamics). Both computer programs have the capability of analyzing horizontal-axis windmill configurations consisting of N blades and, at present, they can predict performance on windmills of various geometries.

Various results obtained with WILSA and WICCA are presented here. The windmill rotor used in obtaining the numerical results has radius $R = 62.5$ ft, root radius $r_{\text{root}} = 0.064R$, root chord $c_{\text{root}} = 0.064R$, tip chord $c_{\text{tip}} = 0.04R$, with a linear variation of the chord in between. The twist angle θ is such that the trailing edge of the windmill surface is tangent to the wind velocity [see Eq. (2)] for a zero-power wind velocity ratio $U_0/\Omega R = 0.0448$. The constant windmill angular velocity is $\Omega = 4.188$ rad/s. This yields

$$\theta = \tan^{-1}\left(\frac{\Omega\,|\boldsymbol{P}_{TE}|}{U_0}\right) \tag{38}$$

The blade twist is around the blade trailing edge, which is parallel to the y-axis.

The wake geometry is helicoidal and automatically adjusts itself for various values of $U_\infty/\Omega R$, i.e., a complete wake spiral extends behind the trailing edge a distance d, given by

$$d/R = 2\pi U_\infty/\Omega R \tag{39}$$

Thus, the wake geometry is described by

$$x = x_{TE} + U_\infty\alpha/\Omega \tag{40a}$$

$$y = \sqrt{y_{TE}^2 + z_{TE}^2}\cos(\alpha + \alpha_{TE}) \tag{40b}$$

$$z = \sqrt{y_{TE}^2 + z_{TE}^2}\sin(\alpha + \alpha_{TE}) \tag{40c}$$

The elements σ_k are automatically generated in a geometry preprocessor. The procedure used is briefly described here.

Consider first the lifting-surface method. First a set of points (x_{jk}, y_{jk}) with

$$x_{jk} = x_{LE}^{(k)} + c^{(k)} (j/N_x)^2 \tag{41a}$$

$$y_{jk} = r_R + (R - r_R)[3(k/N_y)^2 - 2(k/N_y)^3] \tag{41b}$$

$(j = 0, 1, \ldots N_x;\ k = 0, 1, \ldots N_y)$ is generated in the plane $z = 0$. [In Eq. (41), $c^{(k)}$ and $x_{LE}^{(k)}$ indicate the chord and the location of the leading edge for a given blade section.] These expressions yield nonuniform elements; more precisely the elements are smaller near the root, the tip, and the leading edge of the blade. Next, these points are mapped into the corner points of the elements by a rigid body rotation of each section around the trailing edge. Note that the reason for using nonuniform elements on the blade is to obtain a higher rate of convergence. For finite-thickness blades the untwisted blade has symmetric profile with convenient thickness distribution (see Ref. 17). On the other hand, the wake surface is divided into N_s spirals with N_e uniform elements per spiral. Thus, the results depend upon the following parameters of the numerical scheme: the number of elements on the blade along the blade chord N_x, the number of elements along the blade radius N_y, the number of wake spirals N_s, and the number of surface elements per spiral N_e along the flow direction. Thus, an analysis of convergence in the steady state is presented first, in order to find the values of N_x, N_y, N_s, and N_e necessary for a converged $\Delta\phi/U_\infty R$ distribution. Only one blade is used in this analysis, in order to minimize the computation time. The results obtained with WILSA are shown in Figs. 1 to 4 for the convergence analysis. For all of the results $U_\infty/\Omega R = 0.1008$ and $\Omega = 4.188$ rad/s, while the coning angle is equal to zero (the effect of the coning angle is presented in Fig. 6). Similar results obtained with the program WICCA are presented in Ref. 1. The effects of N_e, N_x, N_s, and N_y are given, respectively, in Figs. 1 to 4. All of these figures present the distribution of $\Delta\phi/U_\infty R$ along the blade radius at the centroids of the last row of blade elements. Note that $\Delta\phi/U_\infty R$ at the trailing edge is close to the one at the centroids of the blade elements in contact with the trailing edge. Consider first the effect on $\Delta\phi/U_\infty R$ of the number of elements per spiral, which is shown in Fig. 1. The results are obtained with $N_x = 4$, $N_y = 8$, $N_s = 1$, and $N_e = 6$, 12, 18, and 24. Note that for $N_e = 18$ the solution is practically converged. However, for $N_e = 6$ the results are very close to the converged ones. (Note that the number of elements per spiral is more important on the first spiral than the next ones. Therefore the convergence results obtained with $N_s = 1$ are expected to be valid for any number of spirals.) Hence, $N_e = 6$ is used for the analysis of the effects of N_s, N_x, and N_y. Next, consider the effect of the number of spirals N_s, which is presented in Fig. 2. The results are obtained for $N_x = 4$, $N_y = 8$, $N_e = 6$, and $N_s = 1$, 2, 3, and 4. The solution is practically converged for $N_s = 3$ and this value is used for the analysis of the effects of N_x and N_y.

Next, consider the effect of the number of surface elements on the blade along the chord, which is shown in Fig. 3. The results are obtained with $N_s = 3$, $N_e = 6$, $N_y = 8$, and $N_x = 3$, 4, 5, and 6. Note that, as mentioned earlier, the $\Delta\phi/U_\infty R$ distribution is given at the centroids of the elements in contact with the trailing edge. The locations of these centroids change with N_x. Therefore, the effect of N_x on the convergence is not

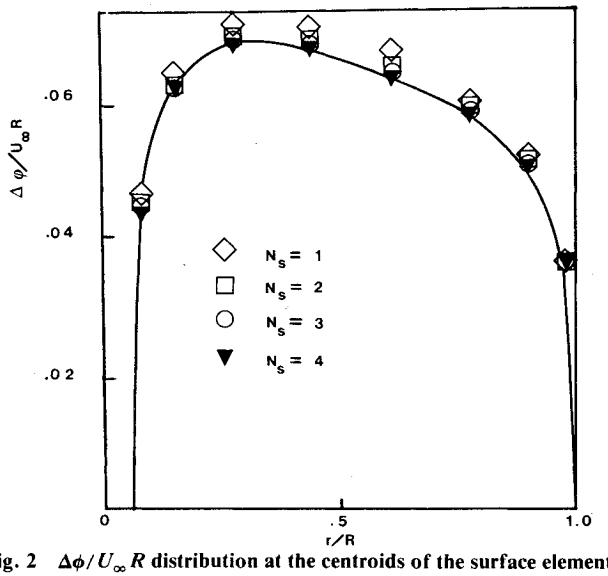

Fig. 2 $\Delta\phi/U_\infty R$ distribution at the centroids of the surface elements in contact with the trailing edge of a one-bladed windmill with $R = 62.5$ ft, $\Omega = 4.188$ rad/s, $r_{root} = 0.064R$, $c_{root} = 0.064R$, $c_{tip} = 0.04R$, $U_0/\Omega R = 0.0448$, $U_\infty/\Omega R = 0.1008$. ($N_x = 4$, $N_y = 8$, $N_e = 6$, $N_s = 1$, 2, 3, and 4.)

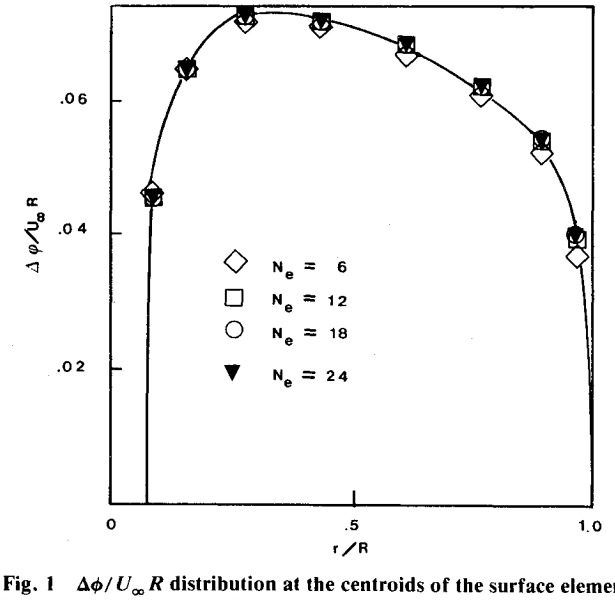

Fig. 1 $\Delta\phi/U_\infty R$ distribution at the centroids of the surface elements in contact with the trailing edge of a one-bladed windmill with $R = 62.5$ ft, $\Omega = 4.188$ rad/s, $r_{root} = 0.064R$, $c_{root} = 0.064R$, $c_{tip} = 0.04R$, $U_0/\Omega R = 0.0448$, $U_\infty/\Omega R = 0.1008$. ($N_x = 4$, $N_y = 8$, $N_s = 1$, $N_e = 6$, 12, 18, and 24.)

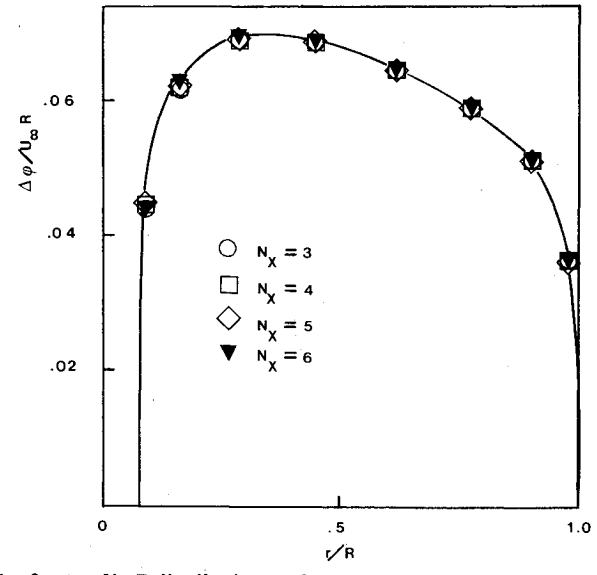

Fig. 3 $\Delta\phi/U_\infty R$ distribution at the centroids of surface elements in contact with the trailing edge of a one-bladed windmill with $R = 62.5$ ft, $\Omega = 4.188$ rad/s, $r_{root} = 0.064R$, $c_{root} = 0.064R$, $c_{tip} = 0.04R$, $U_0/\Omega R = 0.0448$, $U_\infty/\Omega R = 0.1008$. ($N_y = 8$, $N_s = 3$, $N_e = 6$, $N_x = 3$, 4, 5, and 6.)

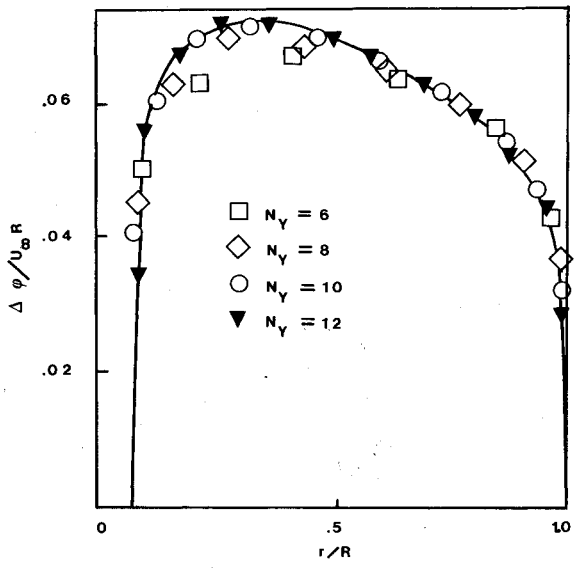

Fig. 4 $\Delta\phi/U_\infty R$ **distribution at the centroids of surface elements in contact with the trailing edge of a one-bladed windmill with** $R=62.5$ **ft,** $\Omega=4.188$ **rad/s,** $r_{root}=0.064R$, $c_{root}=0.064R$, $c_{tip}=0.04R$, $U_0/\Omega R=0.0448$, $U_\infty/\Omega R=0.1008$. ($N_x=4$, $N_s=3$, $N_e=6$, $N_y=6$, 8, 10, and 12.)

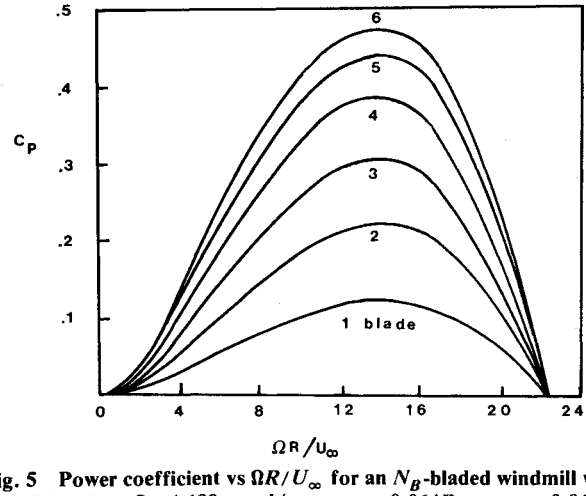

Fig. 5 Power coefficient vs $\Omega R/U_\infty$ **for an** N_B**-bladed windmill with** $R=62.5$ **ft,** $\Omega=4.188$ **rad/s,** $r_{root}=0.064R$, $c_{root}=0.064R$, $c_{tip}=0.04R$, $N_B=1$, 2, 3, 4, 5, 6, $U_0/\Omega R=0.0448$. ($N_x=4$, $N_y=10$, $N_s=3$, $N_e=6$.)

as small as indicated in Fig. 3. However, it should be noted that Fig. 3 may be interpreted in a different way: as N_x tends to infinity the centroids of the elements in contact with the trailing edge tend to the trailing edge; thus, the values of $\Delta\phi/U_\infty R$ presented in Fig. 3 tend to the value of $\Delta\phi/U_\infty R$ at the trailing edge. Thus, Fig. 3 indicates that the values of $\Delta\phi/U_\infty R$ at the centroids of the trailing-edge elements are very close to the converged values of $\Delta\phi_{TE}/U_\infty R$ even for $N_x=3$.

Finally, consider the effect on convergence of N_y, which is presented in Fig. 4. The results are obtained for $N_s=3$, $N_e=6$, $N_x=4$, and $N_y=6$, 8, 10, and 12. The results indicate that for $N_y=10$ the solution is nearly converged.

Next, consider the effects of the number of blades and the coning angle which are presented in Figs. 5 and 6. In both figures the parameters of the problem are $R=62.5$ ft, $c_{root}=0.064R$, $c_{tip}=0.04R$, $r_{root}=0.064R$, $N_x=4$, $N_y=10$, $N_s=3$, and $N_e=6$. The results presented here were obtained with WILSA; similar results were obtained with WICCA. The effect of the number of blades is shown in Fig. 5, which presents the power coefficient as a function of the tip speed to

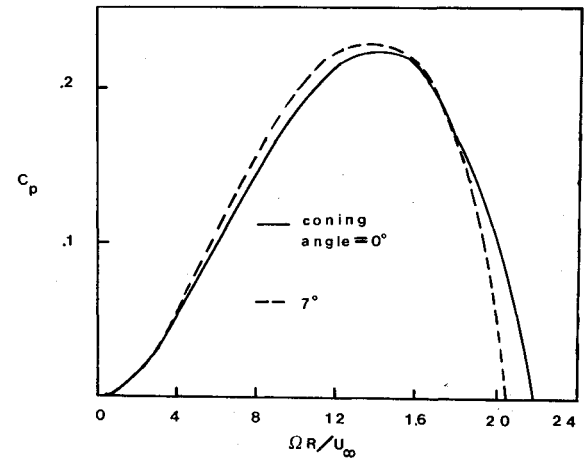

Fig. 6 Power coefficient vs $\Omega R/U_\infty$ **for a two-bladed windmill with coning angle** $\alpha_c=0$ **deg, and 7 deg,** $R=62.5$ **ft,** $\Omega=4.188$ **rad/s,** $r_{root}=0.064R$, $c_{root}=0.064R$, $c_{tip}=0.04R$, $U_0/\Omega R=0.0448$. ($N_x=4$, $N_y=10$, $N_s=3$, $N_e=6$.)

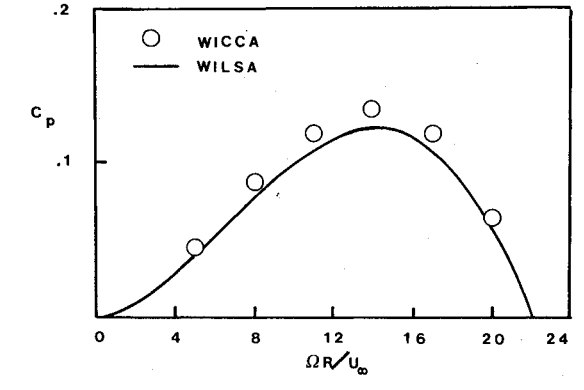

Fig. 7 Power coefficient vs $\Omega R/U_\infty$ **for a one-bladed windmill with** $R=62.5$ **ft,** $\Omega=4.188$ **rad/s,** $r_{root}=0.064R$, $c_{root}=0.064R$, $c_{tip}=0.04R$, $U_0/\Omega R=0.0448$. ($N_x=4$, $N_y=10$, $N_s=3$, $N_e=6$ **for WILSA and** $N_x=3$, $N_y=10$, $N_s=3$, $N_e=6$ **for WICCA.**)

wind speed ratio for a number of blades $N_B=1$, 2, 3, 4, 5, and 6 and zero coning angle. It is apparent that the effect of adding one blade decreases with the number of blades; however, such effect is still important at $N_B=6$. The effect of the coning angle is shown in Fig. 6 which presents the power coefficient for a two-blade rotor as a function of the tip speed to wind speed ratio for a coning angle of 0 and 7 deg, respectively. It is apparent that the effect of the coning angle on the results is very small. Note that 7 deg is the value of the coning angle of the NASA 100-KW windmill. (The geometry used here approximates the NASA 100-KW windmill except for the twist angle.)

A comparison between the two methods is presented in Fig. 7, in which the power coefficient as a function of the tip speed to wind speed ratio is shown. Both curves are for a one-blade rotor with $R=62.5$ ft, $c_{root}=0.064R$, $c_{tip}=0.04R$, $r=0.064R$. The lifting surface (WILSA) results were obtained with $N_x=4$, $N_y=10$, $N_s=3$, and $N_e=6$. The WICCA results were obtained with $N_x=3$, $N_y=10$, $N_s=3$, and $N_e=6$. It should be noted that although the two methods are completely different, the results are very close.

Figures 8 and 9 present a comparison of the present method with the numerical method of Ref. 13 and the experimental data of Ref. 19 for helicopter rotors in hover. The blade geometry employed approximates that of the XH-51A helicopter rotor and is described in Refs. 13 and 19. The present methods use the classical helicoidal wake geometry described in this section with U_∞ replaced by the induced

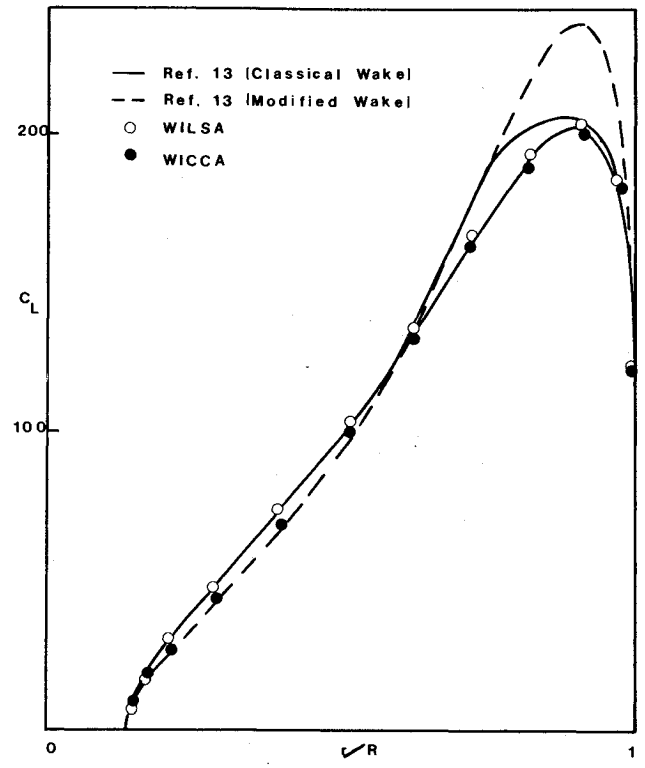

Fig. 8 Section lift coefficient, C_L (lb/ft), vs nondimensional blade radius for a one-blade helicopter rotor in hover.

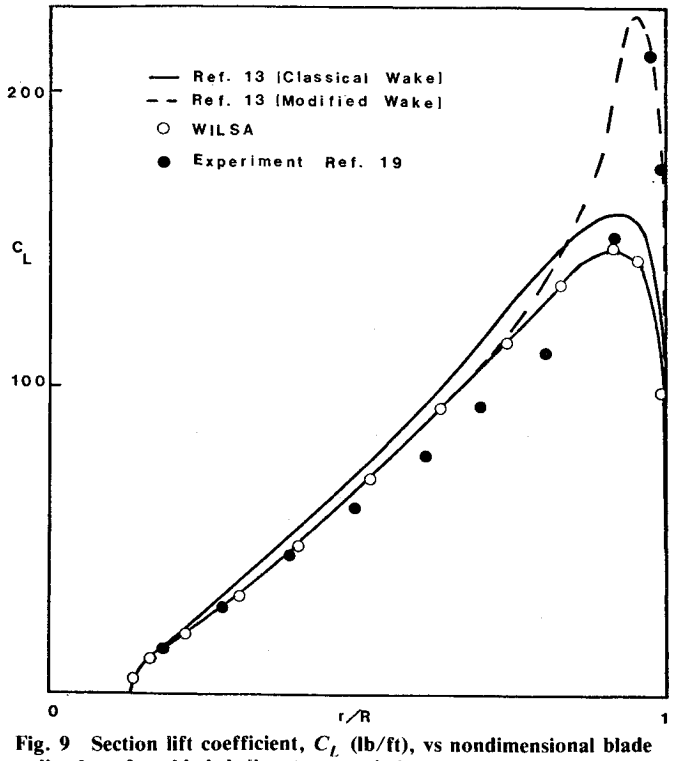

Fig. 9 Section lift coefficient, C_L (lb/ft), vs nondimensional blade radius for a four-blade helicopter rotor in hover.

velocity u, obtained from the expression for the thrust coefficient C_T, which yields

$$u/\Omega R = \sqrt{C_T/2} \tag{42}$$

Figure 8 presents the section lift coefficient as a function of the blade fractional radius for a one-blade helicopter rotor with angular velocity $\Omega = 37.1755$ rad/s and thrust coefficient

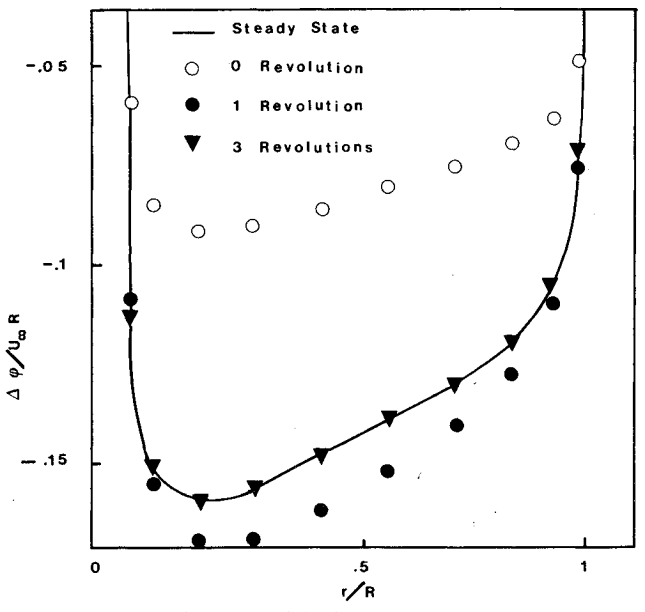

Fig. 10 Perturbation potential discontinuity at trailing edge vs nondimensional blade radius for uniform coaxial flow. Steady and transient analyses.

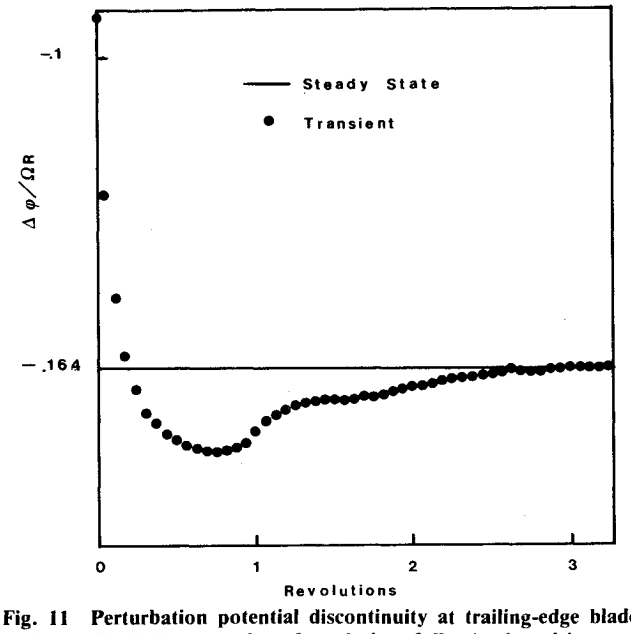

Fig. 11 Perturbation potential discontinuity at trailing-edge blade station, $r/R = 0.21$, vs number of revolutions following impulsive start for uniform coaxial flow. Steady and transient analyses.

(obtained in Ref. 13), $C_T = 0.001860$. Shown is a comparison of the lifting surface (WILSA) method and the complex configuration (WICCA) method with the classical-wake and Landgrebe-wake¶ numerical results of Ref. 13.

The difference between the two classical wake results appears to be due to unnecessary simplifications (in Ref. 13 the normal to the blades is replaced by the normal to the rotor disk) as well as compressibility effects (using local-Mach-number Prandtl-Glauert transformations) which are included in Ref. 13.

Figure 9 presents the section lift coefficient as a function of blade fractional radius for one blade of a four-blade helicopter rotor in hover with angular velocity $\Omega = 37.1755$ rad/s and thrust coefficient (obtained in Ref. 13),

¶The Landgrebe wake is prescribed from experimental data and accounts for concentration of the vorticity into a tip vortex (Ref. 20).

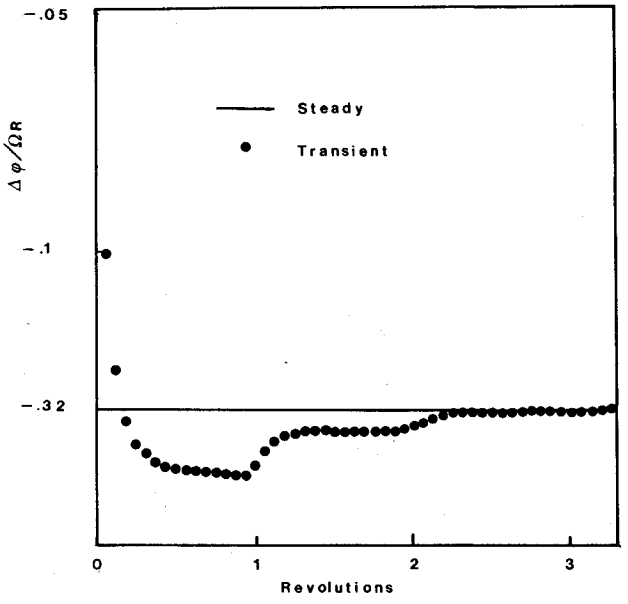

Fig. 12 Perturbation potential discontinuity at trailing-edge blade station, $r/R=0.85$, vs number of revolutions following impulsive start for uniform coaxial flow. Steady and transient analyses.

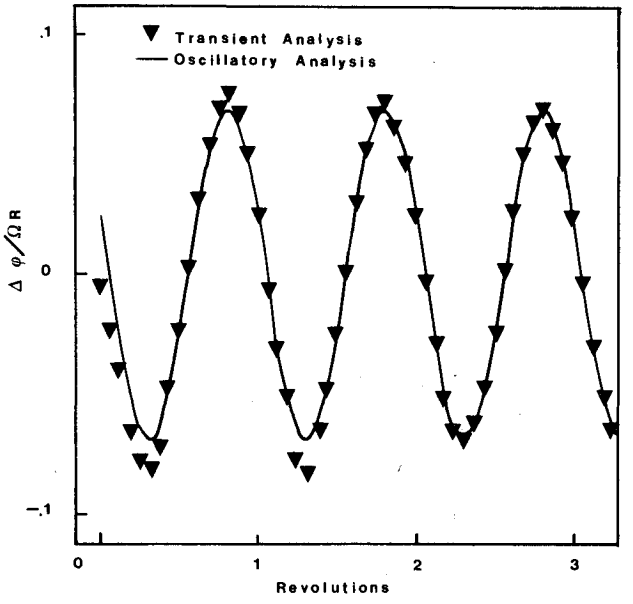

Fig. 14 Unsteady portion of perturbation potential discontinuity at trailing-edge blade section, $r/R=0.21$, vs number of revolutions following instantaneous conversion from uniform to shear wind. Transient and oscillatory analyses.

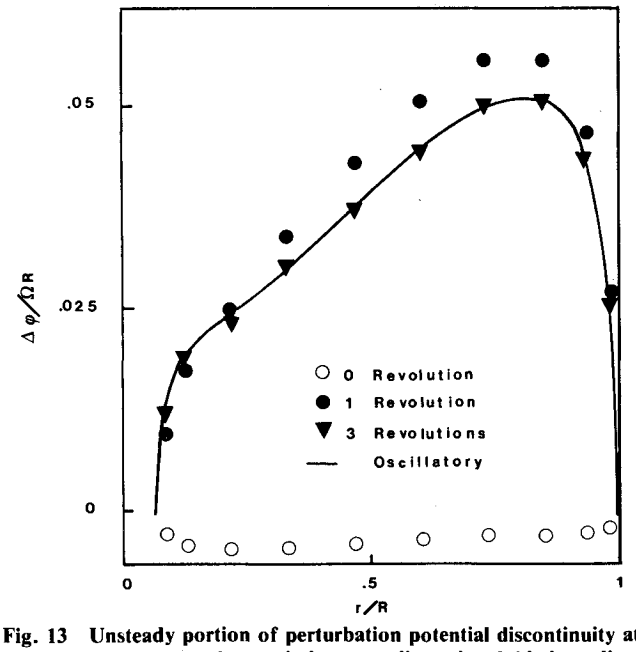

Fig. 13 Unsteady portion of perturbation potential discontinuity at trailing edge due to shear wind vs nondimensional blade radius. Oscillatory and transient analyses.

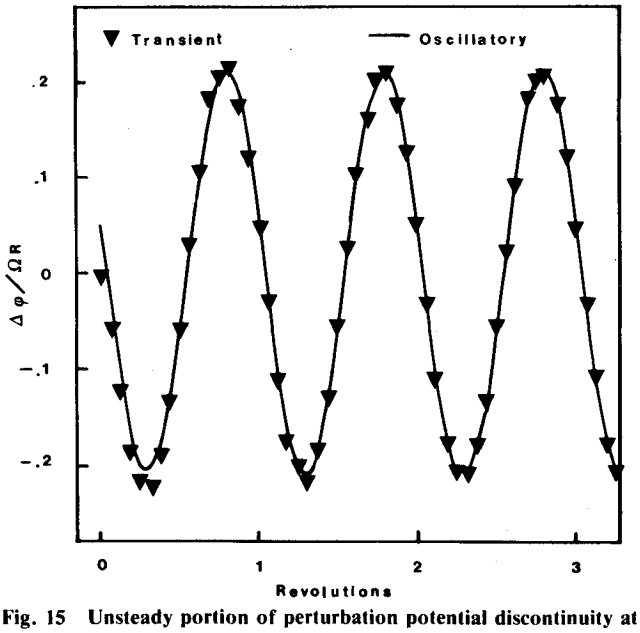

Fig. 15 Unsteady portion of perturbation potential discontinuity at trailing-edge blade station, $r/R=0.85$, vs number of revolutions following instantaneous conversion from uniform to shear wind. Transient and oscillatory analyses.

$C_T=0.005679$. Shown is a comparison of the lifting surface (WILSA) method with the classical-wake and Landgrebe-wake numerical results of Ref. 13 and the experimental results of Ref. 19.

Note that the rotor is lightly loaded so that viscous effects are expected to be negligible. The spike effect near the tip of the blade is clearly demonstrated by the Landgrebe-wake results of Ref. 13 to be due to the concentration of vorticity near the tip.

Figures 10 through 15 present a comparison of the transient and oscillatory analyses in conjunction with the finite-thickness formulation. The blade and wake geometries of this one-blade rotor are the same as those used for the convergence study (Figs. 1-4). The specific parameters used are $R=62.5$ ft, $\Omega=4.188$ rad/s, $U_\infty/\Omega R=0.1008$, $N_x=4$, $N_y=10$, $N_s=3$, $N_e=16$, $U_0/\Omega R=0.0448$, $r_{\text{root}}=0.064R$, $c_{\text{root}}=0.064R$, and $c_{\text{tip}}=0.04R$.

Figures 10-12 present a comparison of the steady-state case with the transition from impulsive start to the steady state. Figure 10 shows the trailing-edge potential discontinuity as a function of blade fractional radius after 0, 1, and 3 revolutions following impulsive start. Figures 11 and 12 show the trailing-edge potential discontinuity at blade stations $r/R=0.21$ and 0.85, respectively, as a function of angular position of the rotor (measured in revolutions following impulsive start). It is apparent that the steady state has been reached after about three revolutions.

Figures 13-15 present a comparison of the oscillatory and transient analyses in the case of a linear coaxial wind shear. Only the unsteady portion of the trailing-edge potential

discontinuity divided by the tangent of the shear angle is shown. This is shown as a function of blade fractional radius in Fig. 13 for 0, 1, and 3 revolutions following instantaneous conversion from steady state to shear wind and is shown at blade stations $r/R=0.21$ and 0.85 in Figs. 14 and 15, respectively, as a function of rotor angular position (measured in revolutions following instantaneous conversion to shear wind).

VII. Conclusions

Two integral-equation methods (for complex configurations and lifting surfaces) for computing the pressure distribution and power coefficients for horizontal-axis windmills in steady and unsteady flows have been described. Agreement between methods is excellent. Comparison with experiment appears to be quite good in the case of helicopter rotors in hover, especially when one considers that the spike effect in Figs. 8 and 9 seems to be due to a more careful description of the wake geometry. Comparison between the oscillatory and transient analyses is excellent.

Both the oscillatory and transient analyses may be applied to either the lifting surface or the complex configuration formulation. While the oscillatory analysis requires that the wake be approximated by one of fixed (time invariant) geometry and is incapable of studying the transition loading between operating states, the transient analysis has no such restrictions.

Acknowledgment

This work was supported by the Department of Energy under contract No. E(49-18)-2415. The authors wish to express their appreciation to the technical monitor, D. Teague of DOE, for discussions and suggestions made in connection with this work.

References

[1] Preuss, R. D., Smolka, S. A., Suciu, E. O., and Morino, L., "Computational Nonpotential Aerodynamics for Windmills in Shear-Winds," Boston University, Boston, Mass., ENGR-CCMP-TR-77-07, Sept. 1977.

[2] Morino, L., "Nonpotential Aerodynamics for Windmills in Shear-Winds," *Proceedings of the Second Workshop on Wind Energy Conversion Systems*, Washington, D.C., June 1975, edited by F. R. Eldridge, NSF-RA-N-75-050, MTR-6970, Sept. 1975.

[3] Rankine, W.J.M., "On the Mechanical Principles of the Action of Propellers," *Transactions of the Institution of Naval Architects*, Vol. 6, 1865, pp. 13-39.

[4] Froude, R. E., "On the Part Played in Propulsion by Differences of Fluid Pressure," *Transactions of the Institution of Naval Architects*, Vol. 30, 1889, p. 390-405.

[5] Froude, R. E., "On the Elementary Relation Between Pitch, Slip, and Propulsive Efficiency," *Transactions of the Institution of Naval Architects*, Vol. 19, 1878, p. 47-65.

[6] Betz, A., "Eine Erweiterung der Schraubenstrahl-Theorie," *Zeitschrift für Flugtechnik und Motorluftschiffahrt*, Vol. 11, 1920, p. 105.

[7] Drzewiecki, S., *Théorie Générale de l'Hélice*, Gauthier-Villars et cie, Paris, 1920.

[8] Glauert, H., "Airplane Propellers," Div. L., Chap. XI, "Windmills and Fans," *Aerodynamic Theory, A General Review of Progress*, edited by W. F. Durand, Vol. 4, Dover, N.Y., 1963, pp. 324-341.

[9] Wilson, R. E. and Lissaman, P.B.S., "Applied Aerodynamics of Wind Power Machines," Oregon State University, Corvallis, Oregon, May 1974.

[10] Wilson, R. E., Lissaman, P.B.S., and Walker, S. N., "Aerodynamic Performance of Wind Turbines," Oregon State University, Corvallis, Oregon, June 1976.

[11] Rohrbach, C., "Experimental and Analytical Research on the Aerodynamics of Wind Turbines," ERDA, Division of Solar Energy, COO-2615-76-T-1, 1975.

[12] Summa, J. M., "Potential Flow about Impulsively Started Rotors," *Journal of Aircraft*, Vol. 13, April 1976, pp. 317-319.

[13] Rao, B. M. and Schatzle, P. R., "Analysis of Unsteady Airloads of Helicopter Rotors in Hover," AIAA Paper 77-159, Jan. 1976.

[14] Suciu, E. O. and Morino, L., "Nonlinear Steady Incompressible Lifting-Surface Analysis with Wake Roll-Up," *AIAA Journal*, Vol. 15, Jan. 1977, pp. 54-58.

[15] Morino, L., "A General Theory of Unsteady Compressible Potential Aerodynamics," NASA CR-2464, Dec. 1974.

[16] Morino, L., Chen, L. T., and Suciu, E. O., "Steady and Oscillatory Subsonic and Supersonic Aerodynamics around Complex Configurations," *AIAA Journal*, Vol. 13, March 1975, pp. 368-374.

[17] Suciu, E. O., Preuss, R., and Morino, L., "Computational Aerodynamic Analysis of Horizontal-Axis Windmills," Boston University, Boston, Mass., ENGR-CCMP-TR-76-01, Sept. 1976.

[18] Preuss, R. D. and Morino, L., "Evaluation of the Doublet Integral for a Hyperboloidal Element," Boston University, Boston, Mass., ENGR-CCMP-TN-76-04, July 1976.

[19] Bartsch, E. A., "In-Flight Measurements and Correlation with Theory of Blade Airloads and Responses on the XH-51A Compound Helicopter Rotor—Volume I: Measurement and Data Reduction of Airloads and Structural Loads," USAAVLABS TR-6822A, May 1968.

[20] Landgrebe, A. J., "An Analytical and Experimental Investigation of Helicopter Rotor Hover Performance and Wake Geometry Characteristics," USAAMRDL Tech. Rept. 71-24, June 1971.